S3–24

Fundamental Research on Aircraft Icing

Xiaomin Wu[1*], *Jingchun Min*[2*], *Xuan Zhang*[1], *Xin Liu*[2]
[1] Department of Energy and Power Engineering, Tsinghua University, Beijing 100084, China
[2] Department of Engineering Mechanics, Tsinghua University, Beijing 100084, China
[*] Corresponding author: Email: wuxiaomin@tsinghua.edu.cn (X.M. Wu), minjc@tsinghua. edu.cn (J. C. Min)

Summary

Aircraft icing presents a serious hazard for flight, which may occur when supercooled droplets in clouds impinge and stick on aircraft. This paper introduces some fundamental research work we have done on aircraft icing. We have recently conducted a series of researches on that subject and obtained many interesting results, the present paper reports some of them, which include the aircraft icing model considering ice property variability and runback water effect, experimental studies on icing nucleation characteristics of sessile water droplets, and modelling of sessile water droplet shape evolution during freezing. These results can provide insights into the aircraft icing and other relevant areas such as frost in refregeration, material solidification, etc.

Keywords: Aircraft icing; Nucleation; Freezing; Supercooled droplet

1. Introduction

Aircraft icing increases drag and reduces lift, even leads to serious flight accidents [1]. On the macro level, developments of theoretical models for aircraft icing can help improve the accuracy of ice accretion prediction, which may act to increase the flight safety [2–4]. On the micro level, the aircraft icing is caused by supercooled droplets in clouds impinging and sticking on aircraft surfaces. Studies on freezing process of a sessile supercooled water droplet may contribute to not only the fundamental understanding of the freezing phenomena [5] but also the improvement of the ice accretion prediction [6].

2. Aircraft Icing Model Considering Ice Property Variability and Runback Water Effect

We claimed in our previous researches [2, 3] that rime ice was actually a kind of porous medium and its effective properties (such as the volume fraction, density, and thermal conductivity) were initially influenced by the airflow parameters and then varied with the rime ice thickness, which affects the ice accretion characteristics as illustrated in Fig. 1(a). Fig. 1(b) shows the basic physical model that consists of the rime ice layer, glaze ice layer, and water film. Density varies linearly along the rime ice thickness but remains constant in the glaze ice layer and water film. Couette flow occurs in the water film, implying that water flows with a linear velocity distribution, through which the runback water effect is considered. More detailed descriptions of the model can be found in our previous papers [2, 3].

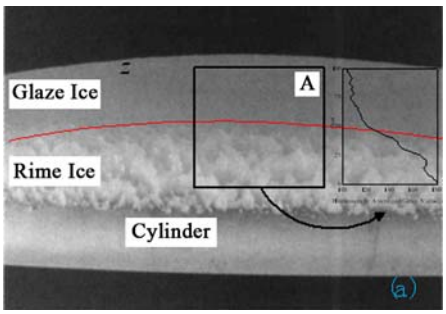

a)

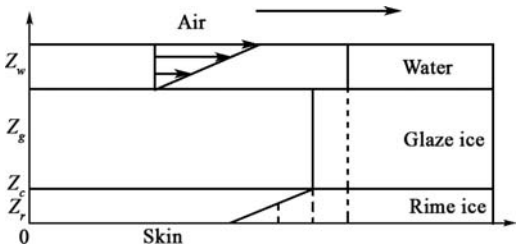

b)

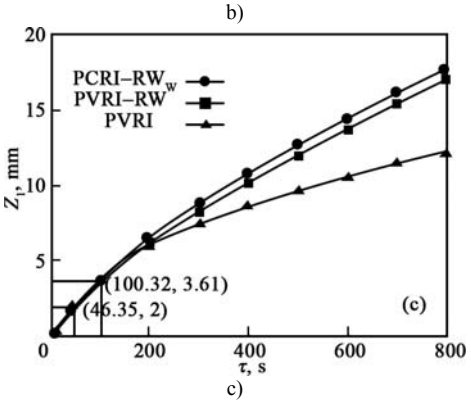

c)

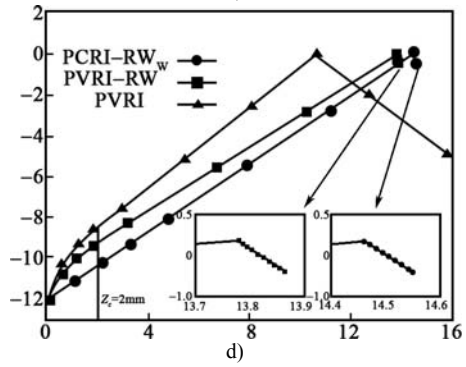

d)

Figure 1. Icing Model: (a) Variations of gray value with ice thickness, (b) Physical model including property–variable rime ice and runback water, (c) Evolutions of ice thicknesses generated by various models. (d) Temperature profiles at $\tau = 600$ s generated by various models. (PVRI: property–variable rime ice, PCRI: property–constant rime ice, RW: runback water)

2.1 Physical properties of rime ice

The initial rime ice density at the skin surface can be expressed as [7],

$$\rho_x = 1\ 000\exp\left[-0.15\times\left(1+\frac{6\ 043}{S^{2.65}}\right)\right] \tag{1}$$

The initial volume fraction and initial effective thermal conductivity of the rime ice, which can be regarded as a kind of porous medium[8].

$$f_{r,\,0} = \frac{\rho_{r,\,0}-\rho_a}{\rho_g-\rho_a} \tag{2}$$

Assuming that the rime ice properties vary linearly with the rime ice thickness, the effective thermal conductivity can be calculated from

$$\begin{aligned} k_r &= k_g\cdot\frac{2k_g+k_a-2(1-f_r)(k_g-k_a)}{2k_g+k_a+(1-f_r)(k_g-k_a)} \approx B_k z + k_{r,\,0} \\ B_k &= \frac{k_g-k_{r,\,0}}{z_c},\ 0\le z\le z_c \end{aligned} \tag{3}$$

2.2 Dry mode icing and critical point

Through derivations, the formulas for the critical time and critical ice thickness can be obtained as follows [2, 3]

$$\begin{aligned} \tau_c &= \frac{(B_\rho z_c+\rho_{r,\,0})^2-\rho_{r,\,0}^2}{2\varphi V\beta B_\rho} \\ z_c &= Z_c\frac{k_g-k_{r,\,0}}{k_g\ln(k_g/k_{r,\,0})} \\ Z_c &= \frac{k_g(t_m-t_s)}{\varphi V\beta L_f+q_{source}-h_e(t_m-t_s)} \end{aligned} \tag{4}$$

2.3 Wet mode icing

In the water film, the flow driven by the air fluid can be simplified as one–dimensional (1d) Couette flow. The 1d momentum and energy equations therefore are

$$\mu_w\frac{d^2v_w}{dz^2}=0,\ \ k_w\frac{d^2t_w}{dz^2}=-\mu_w\left(\frac{dv_w}{dz}\right)^2 \tag{5}$$

At the rime ice/glaze ice interface, the temperature, heat flux, and physical properties of the rime ice are equal to those of the glaze ice. At the glaze ice/water interface and air/water interface, the energy equations satisfy

$$\rho_g L_f\frac{dz_g}{d\tau}=k_g\frac{\partial t_g}{\partial z}-k_w\frac{\partial t_w}{\partial z} \tag{6}$$

$$-k_w\left.\frac{\partial t_w}{\partial z}\right|_{z=z+z_w}=(q_{con}+q_{eva}+q_a)-(q_a+q_k) \tag{7}$$

The velocity profile in water film and the water film thickness are

$$\begin{aligned} v_w &= \frac{F_T}{\mu_w}(z-z_1) \\ z_w &= \sqrt{\frac{2\mu_w G}{\rho_w F_T}}=\sqrt{\frac{2\mu_w\varphi V\beta}{\rho_w F_T}\left(1-\frac{\rho_g}{\varphi V\beta}\frac{dz_g}{d\tau}\right)} \end{aligned} \tag{8}$$

The relation between the glaze ice thickness and time can be obtained as

$$\rho_g L_f\frac{dz_g}{d\tau}=k_g\frac{\partial t_g}{\partial z}-k_w\frac{\partial t_w}{\partial z}=k_g\frac{t_m-t_p}{z_g}-k_w\frac{t_{aw}-t_m}{z_w}+\frac{z_w F_T^2}{2\mu_w} \tag{9}$$

2. 4 Basic ice accretion characteristics

Calculations are made for MVD=20μm, V=60m/s, φ=1g/m^3, β=0.55, t_a=t_s=−12°C and t_m=0°C, these parameters are taken based on the data in Ref. [9]. The results generated by the PCRI–RW, PVRI–RW, and PVRI models are presented in Figure 1(c) and 1(d).

In Fig. 1(c), the asterisks express the critical point. The critical time and critical ice thickness given by the PVRI model are the same as those by the PVRI–RW model because they share the same dry mode icing stage. However, the PVRI–RW model yields a shorter critical time and a smaller critical ice thickness than the PCRI–RW model because the PVRI–RW model treats the rime ice as a porous medium that has a smaller effective thermal conductivity and density than the glaze ice while the PCRI–RW model treats the rime ice as the glaze ice and assumes that the rime ice has the same properties as the glaze ice at constant.

In Fig. 1(d), the rime ice temperature profiles generated by the PVRI and PVRI–RW models are logarithmic curves due to the variations of the rime ice physical properties with the ice thickness while that by the PCRI–RW model is a straight line. The water film temperature profiles given by these three models differ from one another due to different water film thicknesses. The water film temperature profiles given by the PVRI–RW and PCRI–RW models both are parabolic.

More results and further discussion can be found in our previous papers [2, 3].

3. Experimental Studies on Icing Nucleation Characteristics of Sessile Water Droplets

Since the aircraft icing is caused by the supcooled water droplet in coulds, it is nesseary to study the feezing process of a supercooled sessile water droplet. Such a process can be divided into five distinct stages, as shown by Fig. 2(a): (1) liquid cooling (supercooling), (2) nucleation, (3) recalescence, (4) freezing, and (5) solid cooling [10, 11]. At the nucleation/recalescence stage which is the starting point of the freezing stage, the droplet volume and physical properties change sharply, which may significantly influence the subsequent freezing stage. Here, water droplet nucleation experiments are conducted to investigate the effects of droplet size and time on the nucleaction characteristics.

Fig. 2(b) indicates that the ice nucleation in a supercooled droplet is a random process and the nucleation temperature data scatter over a wide range of temperature. As the droplet becomes smaller, the nucleation temperature data scatter more widely, with its average becoming lower. Fig. 2(c) suggests that the variation of the nucleation probability with the nucleation temperature basically satisfies a normal distribution. A smaller droplet tends to have a higher frozen droplet fraction for a given temperature. The average nucleation temperature decreases and the standard deviation increases as the droplet volume decreases. The average nucleation temperatures are −15.82, −17.04 and −18.33°C for droplets having volumes of 10, 5 and 1 μL with standard deviations of 1.72, 1.92 and 2.46°C.

As shown in Fig. 2(d), for a given volume droplet, the nucleation rate becomes larger as the nucleation temperature decreases because there are more critical nuclei inside the droplet and at the solid–liquid or gas–liquid interface for a larger supercooling degree. For a given temperature, a larger droplet yields a higher nucleation rate because they have more critical nuclei and more nucleation sites than a small droplet.

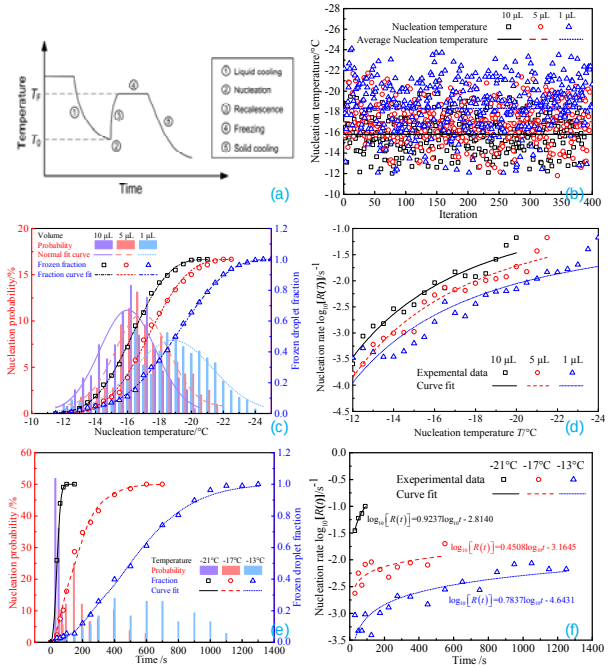

Figure 2. Supercooled droplet nucleation characteristics: (a) Temperature transition at five stages during droplet freezing [12–14], (b) Nucleation temperature, (c) Nucleation probability and frozen droplet fraction sorted by nucleation temperature, (d) Variations of nucleation rate with time of water droplets with different volumes, (e) Nucleation probability and frozen droplet fraction sorted by nucleation time, (f) Variations of the nucleation rate with time of 5 μL water droplets at different temperatures.

As shown in Fig. 2(e), the nucleation time corresponding to the highest nucleation rate shifts toward longer time as the temperature increases, which is consistent with the average nucleation time trend. Figure 2(f) indicates that for a given temperature, the nucleation rate increases slowly with time, which suggests that the transient nucleation differs from quasi–steady nucleation in which the time effects can be neglected.

4. Modelling of Sessile Water Droplet Shape Evolution during Freezing

For the droplet freezing process, the experimental results in Fig. 3(a) [13] shows that the freezing front advances as time passes, and the droplet expands during freezing, which occurs in the droplet above the freezing front. At any moment when the freezing front advances, the angle between the droplet–air interface and the freezing front at the three–phase line remains unchanged, as a result, the profiles of the droplet before and after the occurrence of solidification near the freezing front maintain coincident. The freezing front becomes invisible when it approaches the droplet top at about t = 8.0 s, and a tip with an angle of about 140° eventually forms at t = 8.7 s.

Fig. 3(b) depicts the evolutions of droplet volume and height [13]. As time goes by, the droplet volume and height both increase. The droplet volume increases sharply at the nucleation and recalescence stages and reaches a value of 10.16 μL at the end of the recalescence stage (t=0.1 s), i.e. a 1.6% increase in volume relative to the initial droplet at t=0 s. The volume fraction of ice in the ice–water mixtures corresponding to this volume increment is 19.7%.

Based on the above results, a theoretical model is established to model the freezing process with consideration of supercooling effect as shown by Fig. 3(c) and 3(d).

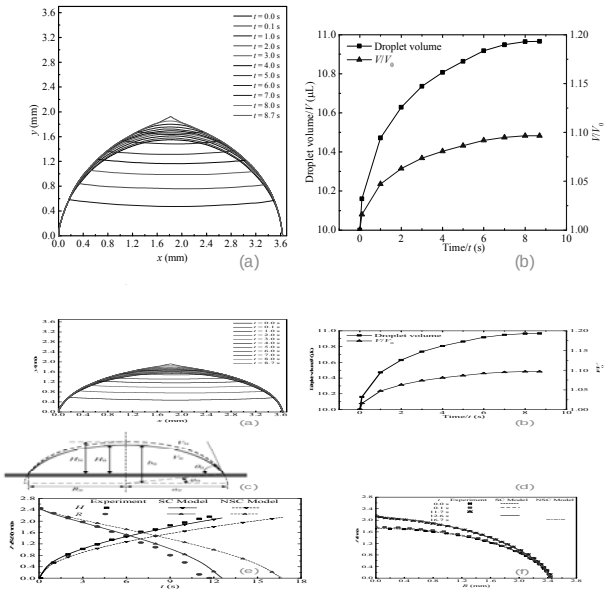

Figure 3. Freezing characteristics: (a) Evolutions of droplet profile and freezing front during freezing process of a 10 μL water droplet, (b) Evolutions of droplet volume during freezing process, (c) Droplet at nucleation/recalescence stage, (d) Droplet during freezing stage, (e) Comparison of the evolutions of freezing front height and radius obtained from the experiment and the SC and NSC models, (f) Comparison of initial and final droplet profiles obtained from the experiment and the SC and NSC models. (SC – supercooling, NSC – no supercooling)

4.1 Initial droplet profile under gravity

The importance of the gravitational force relative to the surface tension force can be measured by the Bond number, which is defined by $Bo=\Delta\rho g D^2/\sigma$. When Bo << 1, the gravity is negligible; otherwise, the gravity may force a sessile droplet to deviate from a spherical cap [15]. In the present research, the Bond number is calculated to be 3 for a 20 μL droplet, meaning that the gravity effect on the droplet shape cannot be neglected. The initial droplet profile under gravity can be described by the Young–Laplace equation as

$$\frac{z''}{(1+z')^{3/2}}+\frac{z'}{x(1+z')^{1/2}}=\frac{2}{b}+\frac{\Delta\rho g z}{\sigma} \qquad (10)$$

4.2 Droplet profile after nucleation/recalescence stage

The ice mass fraction (β_i) after the nucleation/recalescence stage can be calculated from the energy balance, i.e.

$$\beta_i = \frac{c_{w,\,T_s}(T_F - T_N)}{L} = \frac{c_{w,\,T_s}}{c_1} St \tag{11}$$

where T_F–T_N denotes the supercooling degree, and St expresses the Stefan number, given by $St=c_i(T_F–T_N)/L$, which is the ratio of the sensible to latent heat. So, the latent heat of solidification and the thermophysical properties of the water–ice mixture including the density, specific heat and thermal conductivity at the end of the nucleation/recalescence stage can be calculated from

$$L_m=(1–b_i)L \tag{12}$$

while the droplet volume at the end of the nucleation/recalescence stage can be obtained from

$$V_N = \frac{\rho_w V_0}{\rho_m} \tag{13}$$

The droplet profile including the height (H_N) after the nucleation/recalescence stage can thus be figured out, it serves as the initial parameters for the subsequent freezing stage.

4.3 Final droplet profile

Our previous paper [14] presents a theoretical model for calculating the droplet profiles, which takes into account the nucleation/recalescence stage. At the freezing stage, the mass conservation between the water–ice mixture and ice yields

$$\rho_m \frac{dV}{dt} = -\pi\rho_i R^2 \frac{dH}{dt} \tag{14}$$

Since the water–ice mixture remains at a constant temperature of 0°C (freezing point) and the heat conduction in the ice layer is quasi–steady with the in–layer temperature satisfying an approximately linear distribution, the energy conservation at the freezing front, which constitutes a Stefan problem, can be described by

$$\rho_m \frac{dV}{dt} = -\pi\rho_i R^2 \frac{dH}{dt} \tag{15}$$

The trigonometry at the tri–junction illustrated in Fig. 3(d) shows that the decreasing rate of the freezing front radius can be related with the freezing rate (v) and the dynamic contact angle as below

$$\frac{dR}{dt} = -\frac{1}{\tan(\theta-\theta_D)}\frac{dH}{dt} = -\frac{v}{\tan(\theta-\theta_D)} \tag{16}$$

The horizontal slipping velocity (v_S) at the tri–junction can further be related to the freezing rate (velocity) by

$$v_S = v\left(\frac{1}{\tan(\theta-\theta_D)} - \frac{1}{\tan\theta}\right) \tag{17}$$

According to Anderson et al. [16], the slipping velocity can also be related to the contact angle as

$$v_S = \begin{cases} \dfrac{\eta(\theta_R-\theta)}{\theta}, & \theta < \theta_R \\ 0, & \theta \ge \theta_R \end{cases} \tag{18}$$

in which θ_R is the receding angle and η is the characteristic slipping velocity, both of which are empirical parameters that need to be determined by experiments.

The final droplet profile after the freezing process can be obtained from the above model. More detailed descriptions of the model can be found in our previous paper [14].

4.4 Comparison of theoretical and experimental results

Fig. 3(e) compares the evolutions of the freezing front height (H) and radius (R) obtained from the experiment and calculated by the SC and NSC models. As time goes by, the freezing front height increases while the freezing front radius decreases. The results given by the SC model agree better with the experimental data than those by the NSC model. The freezing time obtained from the experiment is 11.7 s, and that calculated by the SC model is 12.6 s, the deviation is 12.6%, while that by the NSC model is 16.7 s, the deviation is as large as 42.7%. So, the SC model can better predict the experiment than the NSC model. The reason is that the SC model takes into account the supercooling effect on the physical properties especially the latent heat. The supercooling degree drives the droplet to change from water into an ice–water mixture at the nucleation/recalescence stage, which has a smaller latent heat than the water, causing an accelerated freezing process and consequently a shorter freezing time.

Fig. 3(f) compares the initial and final droplet profiles obtained from the experiment and calculated by the SC and NSC models. The initial profiles include the profile at the beginning of the nucleation/recalescence stage (t=0 s) and that at the ending of such a stage (t=0.1 s). Both initial profiles look closer to a spherical crown, with that at t=0.1 s being slightly higher than that at t=0 s, because some water changes into ice at t=0.1 s, which has a larger volume than water of the same mass. The final profile has the largest height, because all water changes into ice at the end of the freezing stage. The SC and NSC models provide similar results on the final profile, which agree well with the experimental observations. The NSC model actually yields a little bit different final profile from the SC model, i.e. the former gives a slightly smaller radius at the early freezing stage but a somewhat larger radius at the later stage than the latter. This can be explained from the slope of the droplet profile expressed by $\mathrm{d}H/(-\mathrm{d}R) = \tan(\theta-\theta_\mathrm{D})$. The conical tip angles calculated by the SC and NSC models are both 146°, as compared to 141° of the experimental data, so the calculations agree well with the experiments.

More results and further discussion can be found in our previous paper [14].

5. Conclusions

An improved aircraft icing model named the PVRI–RW model has been developed to simulate the ice accretion process, the model indicates that the rime ice physical properties and

runback water effect are affected by the airflow parameters, they all influence the heat conductions in the ice layer and water film as well as the ice accretion process.

Experimental nucleation results show that supercooled water droplet nucleation is a random process, with the nucleation temperature scattering over a wide range of temperature that approximates a normal distribution. The nucleation rate increases with decreasing nucleation temperature and with increasing droplet size.

A model that considers both the supercooling effect on the latent heat and the gravity effect on the droplet shape has been developed to simulate the freezing behaviors of a water droplet on a cold plate. The supercooling degree significantly affects the droplet freezing process, with a larger supercooling degree causing a more obvious difference in the freezing rate and time between the models with and without consideration of the supercooling effect.

Acknowledgement

This research is funded by National Key Basic Research Program of China (No. 2015CB755800).

References

1. Cao Y.H., Wu Z.L., Su Y. & Xu Z.D., 2015. Aircraft flight characteristics in icing conditions. *Prog. Aerosp. Sci.*, 74. 62–80.

2. Zhang X., Wu X.M. & Min J.C., 2017. Aircraft icing model considering both rime ice property variability and runback water effect. *Int. J. Heat Mass Transfer*, 104, 510–516.

3. Zhang X., Min J.C. & Wu X.M., 2016. Model for aircraft icing with consideration of property–variable rime ice. *Int. J. Heat Mass Transfer*, 97, 185–190.

4. Saeed F., 2002. State–of–the–art aircraft icing and anti–icing simulation. ARA J., 2000–2002(25–27), 106–113.

5. Jung S., Tiwari M.K., Doan N.V. & Poulikakos D., 2012. Mechanism of supercooled droplet freezing on surfaces. *Nat. Commun.*, 3, 615.

6. Alizadeh A., Yamada M., Li R., et al., 2012. Dynamics of ice nucleation on water repellent surfaces. Langmuir, 28(6), 3 180–3 186.

7. Rios M., 1991. Icing simulations using Jones' density formula for accreted ice. Reno, Nevada, *29th Annual Aerospace Sciences Meetin*g.

8. Aichlmayr H.T. & Kulacki F.A., 2006. The effective thermal conductivity of saturated porous media. Advances in Heat Transfer, 39, 377–460.

9. Shin J. & Bond T.H., 1992. Results of an icing test on a NACA 0012 airfoil in the NASA Lewis Icing Research Tunnel, NASA TM–105374/AIAA–92–0647. Cleveland, Ohio, *30th Aerospace Sciencs Meeting and Exhibit.*

10. Fukusako S. & Yamada M., 1993. Recent advances in research on water–freezing and ice–melting problems. *Exp. Therm Fluid Sci.*, 6(1), 90–105.

11. Li F.F. & Liu J. 2010. Thermal infrared mapping of the freezing phase change activity of micro liquid droplet. *J. Therm. Anal. Calorim*, 102(1), 155–162.

12. Chaudhary G. & Li R., 2014. Freezing of water droplets on solid surfaces. An experimental and numerical study. *Exp. Therm Fluid Sci.*, 57, 86–93.

13. Zhang X., Wu X.M & Min J.C., 2017. Freezing and melting of a sessile water droplet on a horizontal cold plate. *Exp. Therm Fluid Sci.*, 88. 1–7.

14. Zhang X., Wu X., Min J. & Liu X., 2017. Modelling of sessile water droplet shape evolution during freezing with consideration of supercooling effect. *Appl. Therm. Eng.*, 125. 644–651.

15. Chatterjee J., 2003. Limiting conditions for applying the spherical section assumption in contact angle estimation. *J. Colloid Interface Sci.*, 259(1). 139–147.

16. Anderson D.M., 1996. Worster M.G., & Davis S.H., The case for a dynamic contact angle in containerless solidification. J. Cryst. Growth, 63(3). 329–338.